

The Role of Sea-ice Processes on the Probability of AMOC Transitions

René M. van Westen,^a Valérian Jacques-Dumas,^a Amber A. Boot,^a Henk A. Dijkstra,^a

^a*Institute for Marine and Atmospheric research Utrecht, Department of Physics, Utrecht University, Princetonplein 5, Utrecht, 3584 CC, the Netherlands*

arXiv:2401.12615v1 [physics.geo-ph] 23 Jan 2024

Corresponding author: René M. van Westen, r.m.vanwesten@uu.nl

ABSTRACT: Recent simulations performed with the Community Earth System Model (CESM) have suggested a crucial role of sea-ice processes in AMOC hysteresis behaviour under varying surface freshwater forcing. Here, we further investigate this issue using additional CESM simulations and a novel conceptual ocean-sea-ice box model. The CESM simulations show that the presence of sea ice gives rise to the existence of statistical equilibrium states with a weak AMOC strength. This is confirmed in the conceptual model, which captures the same AMOC hysteresis behaviour as in the CESM simulation and where steady states are computed versus forcing parameters. In the conceptual model, transition probabilities between the different equilibrium states are determined using rare event techniques. The transition probabilities from a strong AMOC state to a weak AMOC state increase when considering sea-ice processes and indicate that sea ice promotes these transitions. On the other hand, sea ice strongly reduces the probabilities of the reverse transition from a weak AMOC state to a strong AMOC state and this implies that sea ice also limits AMOC recovery. The results here indicate that sea-ice processes play a dominant role in AMOC hysteresis width and influence transition probabilities between the different equilibrium states.

SIGNIFICANCE STATEMENT: We develop a novel conceptual ocean-sea-ice box model to explain AMOC hysteresis behaviour recently found in the Community Earth System Model and determine how sea-ice processes influence the hysteresis width and the probability of AMOC transitions.

1. Introduction

The Atlantic Meridional Overturning Circulation (AMOC) plays an important role in regulating the global climate by redistributing heat and salinity through the global ocean. The effects of anthropogenic climate change on the AMOC provide reasons for concern as the AMOC is a tipping element in the climate system (Armstrong McKay et al. 2022). There is an ongoing debate whether the present-day AMOC is close to its tipping point (Boers 2021; Ditlevsen and Ditlevsen 2023; Mehling et al. 2023), but it is known that AMOC tipping has severe global climate impacts (Orihuela-Pinto et al. 2022; van Westen et al. 2024). So far, historical AMOC reconstructions indicate that its strength is declining since 1900 (Caesar et al. 2018, 2021) and projections of climate models indicate that this decline will continue under future climate change and its decline is insensitive to the used emission scenario (Weijer et al. 2020).

The potential tipping of the AMOC has been studied in a hierarchy of models (Dijkstra 2023), from simple box models (Stommel 1961; Cessi 1994; Cimadoribus et al. 2014), ocean-only models (Dijkstra 2007), to various Earth system Models of Intermediate Complexity (EMICs) (Rahmstorf et al. 2005), early Global Climate Models (GCMs) (Hawkins et al. 2011; Hu et al. 2012), and in modern Earth System Models (ESMs) (Jackson et al. 2022). In box models and ocean-only models, steady state calculations have shown that multi-stable AMOC regimes can exist. Transitions between strong and collapsed AMOC states are caused by the salt-advection feedback, where a freshwater anomaly in the North Atlantic weakens the AMOC strength and reduces the associated salinity transport. This response then amplifies the original freshwater anomaly (Marotzke 2000). In EMICs and ESMs, an impression of such a multi-stable regime can be obtained by slowly increasing the surface freshwater forcing to induce an AMOC collapse. When reversing the surface freshwater forcing, the AMOC often recovers at smaller values of this forcing compared to the collapse, giving rise to hysteresis behaviour (Rahmstorf et al. 2005; Hawkins et al. 2011; Hu et al. 2012).

The presence of a multi-stable AMOC in a hierarchy of models, and possibly in the actual climate system, has far reaching consequences. When the present-day AMOC is in such a regime, there is a finite probability of a noise-induced transition between the different equilibrium states, given the presence of stochastic surface forcing. This probability will increase when approaching the tipping point; in addition, rate-induced transitions may occur (Ashwin et al. 2012; Lohmann and Ditlevsen 2021). Transition probabilities between the different AMOC states, which may arise under stochastic surface freshwater flux noise, have so far been only studied in idealised models (Castellana et al. 2019; Baars et al. 2021). For state-of-the-art climate models determining transition probabilities is problematic since this is computationally very expensive, in particular when the transition probabilities are very low (Jacques-Dumas et al. 2023).

This study is motivated by recent results where such hysteresis behaviour was found in the Coupled Model Intercomparison Project phase 5 (CMIP5) version of the Community Earth System Model (CESM) (van Westen and Dijkstra 2023; van Westen et al. 2024). The transition (‘collapse’) between the strong (‘AMOC on’) to the weak (‘AMOC off’) state was very similar to the one expected from ocean-only models (Dijkstra 2007), whereas the reverse transition (‘recovery’) behaved quite differently. It was shown that sea-ice ocean interactions play an important role in the AMOC recovery because the relatively weak (<5 Sv, $1 \text{ Sv} = 10^6 \text{ m}^3 \text{ s}^{-1}$) northward overturning cell in the Atlantic Ocean is strongly suppressed by the extensive North Atlantic sea-ice cover (van Westen and Dijkstra 2023). However, the precise effects of the sea ice on the multi-stable AMOC regime could not be investigated in CESM, where the surface freshwater forcing was transient.

In this paper, we show that the sea ice actually increases the hysteresis width in the CESM and explain the physics of this result using a novel conceptual ocean-sea-ice model. Using this conceptual model, we also extend the study of Castellana et al. (2019) by looking at transition probabilities between the different equilibrium AMOC states in the presence of sea ice. The conceptual ocean-sea-ice model is described in Section 2. Next in Section 3, we first present additional CESM results and then analyse the steady states and transitions between the steady states in the conceptual model. Finally in Section 4, we summarise and discuss the results.

2. Models and Methods

a. CESM configuration

In van Westen and Dijkstra (2023), version 1 of the CESM was used, with horizontal resolutions of 1° for the ocean/sea ice and 2° for the atmosphere/land components. The CESM simulation was initialised from the end of a 2,800-year long pre-industrial control simulation (Baatsen et al. 2020) under constant greenhouse gas, solar and aerosol forcings set to pre-industrial levels. The hysteresis behaviour in the CESM (van Westen and Dijkstra 2023) was obtained by varying the surface freshwater forcing (F_H) between latitudes 20°N and 50°N in the Atlantic Ocean. This freshwater flux anomaly was compensated over the rest of the domain to conserve salinity, this a typical set-up for a hosing experiment. The surface freshwater forcing linearly increased in time with a rate of $3 \times 10^{-4} \text{ Sv yr}^{-1}$ up to a maximum of $F_H = 0.66 \text{ Sv}$ in model year 2,200. This rate of change in F_H is quite small with the aim to stay close to equilibrium, often referred to as a so-called quasi-equilibrium approach (Rahmstorf et al. 2005; Hu et al. 2012). At the end of the simulation the forcing was reversed and F_H decreased at the same rate and reaches zero in model year 4,400.

The different AMOC states in van Westen and Dijkstra (2023) are not in statistical equilibrium (Hawkins et al. 2011), given the quasi-equilibrium approach, and therefore we performed additional CESM simulations under fixed freshwater forcing values. From the hysteresis simulation we branch off 4 simulations from model years 600 and 3,800 ($F_H = 0.18 \text{ Sv}$) and from model years 1,500 and 2,900 ($F_H = 0.45 \text{ Sv}$), and keep the value of F_H constant during each simulation. The AMOC collapse (recovery) occurs around model year 1,750 (4,100), this motivates the branching points from $F_H = 0.45 \text{ Sv}$ ($F_H = 0.18 \text{ Sv}$). The branched simulations are integrated for 500 years and we determine their statistical properties over the last 50 years.

b. A conceptual ocean-sea-ice model

The new model is based on the ocean box model which was developed by Cimadoribus et al. (2014) and extended by Castellana et al. (2019) (hereafter called CCM, see Figure 1). The CCM consists of conservation equations for the salinity content of boxes s , ts , t and n , one equation to conserve salinity (from which the salinity of box d is derived) and one equation for the time-varying

pycnocline depth (D). The AMOC strength in the northern box (q_N) is given by

$$q_N = \eta \frac{\rho_n - \rho_{ts}}{\rho_0} D^2, \quad (1)$$

where η is a downwelling (pumping) constant, $\rho_n - \rho_{ts}$ is the density difference between box n and box ts and ρ_0 is a reference density. The densities are determined from a linear equation of state. In the CCM, the temperatures for box n and box ts are input parameters (5°C and 10°C, respectively) and are fixed in time. The main forcing parameter is the asymmetric freshwater flux (E_A) from box s to box n. Note that the hosing set-up in the CCM is slightly different than in the CESM where fresh water is added between 20°N and 50°N and compensated elsewhere. Under large E_A , the density difference $\rho_n - \rho_{ts}$ becomes negative and the circulation reverses (red dashed arrows become red dotted arrows in Figure 1). The CCM is extensively discussed in Castellana et al. (2019) and, as we use it for comparison to the new model where sea ice is included, the governing equations and input parameter settings are provided in the Appendix (see equations A1).

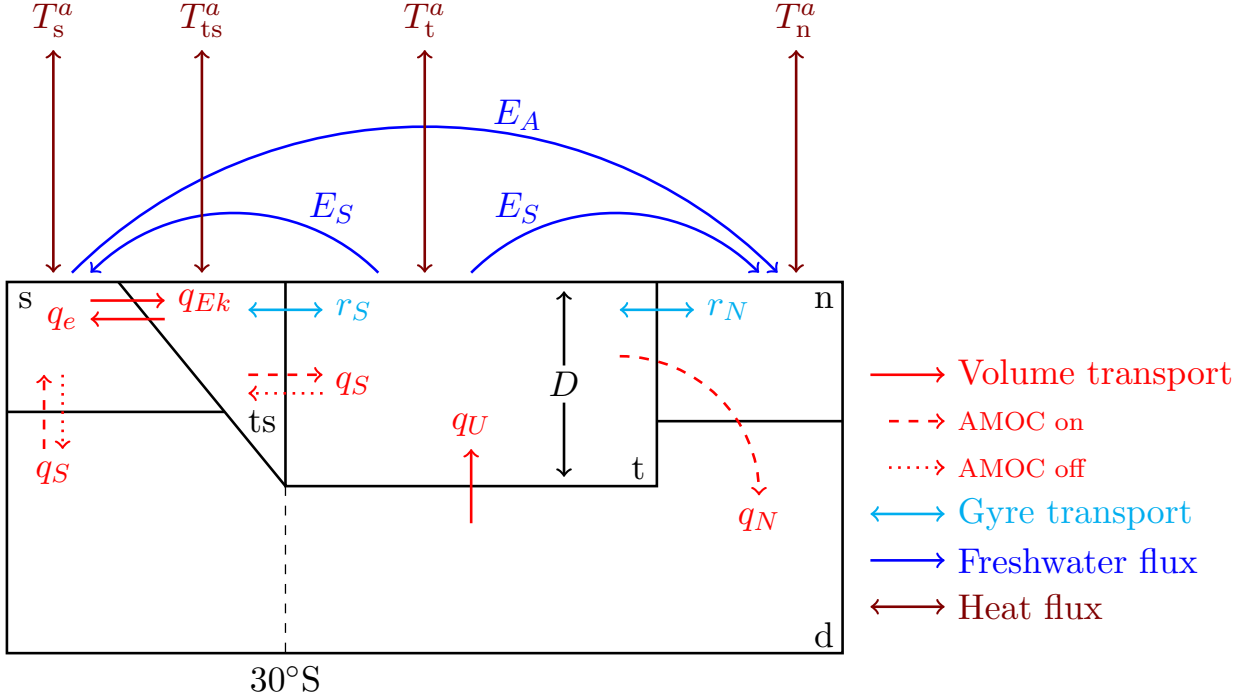
Our aim is to couple sea-ice processes to the CCM and hence we first extend it by including oceanic temperatures. The governing equations for temperature (see equations A2 in the Appendix) are very similar to the ones for salinity. The main difference is that the equations for the surface boxes (box s, ts, t and n) have one additional term which represents the heat exchange with the atmosphere (brown arrows in Figure 1). The change in ocean heat content for each surface box ($i = s, ts, t$ and n) and box d is then given by (under the assumption of constant heat capacity and reference density):

$$\frac{d(V_i T_i)}{dt} = F_i - \lambda^a A_i (T_i - T_i^a), \quad (2a)$$

$$\frac{d(V_d T_d)}{dt} = F_d. \quad (2b)$$

Here, F_i is the advective oceanic heat transport, V_i the volume, A_i the horizontal surface area, λ^a the heat exchange rate with the atmosphere, T_i the ocean temperature and T_i^a the overhead atmospheric temperature. Note that the temperature for box d is a dynamical quantity whereas the salinity of this box is diagnostically derived from salinity conservation.

The heat exchange rate λ^a and atmospheric temperatures are additional parameters in the extended CCM (hereafter E-CCM) that need to be tuned (Appendix and Figure A1). For an arbitrary value



1 FIG. 1. Schematic representation of the 5-box AMOC model, adapted from Cimadoribus et al. (2014) and
 2 Castellana et al. (2019) (the CCM). The red arrows represent the volume fluxes, whereas the dashed and dotted
 3 arrows indicate the AMOC on and AMOC off states, respectively. The cyan and blue arrows are the gyre transport
 4 and freshwater fluxes. The brown arrows are the heat fluxes with the overhead atmosphere for each surface box
 5 (i.e., box s, ts, t and n).

of E_A (and for the AMOC on state), we tune these parameters such that the ocean temperatures for box n and box ts are 5°C and 10°C , respectively. We mainly use $\lambda^a = 3.5 \times 10^{-6} \text{ m s}^{-1}$ below and for the given E_A the AMOC on state of the E-CCM is identical to that of the CCM. We used $E_A = 0.0644 \text{ Sv}$ for tuning and varying this tuning value slightly shifts the bifurcation points in the E-CCM. In the CCM this is the minimum value of E_A for which the freshwater transport carried by the AMOC at 30°S , below indicated by F_{ovS} , becomes negative (Castellana et al. 2019). The quantity F_{ovS} is determined from the model as

$$F_{\text{ovS}} = -\frac{q_S}{S_0} (S_{\text{ts}} - S_d), \quad (3)$$

where S_0 is a reference salinity. The quantity F_{ovS} is important as it is a measure for the salt-advection feedback strength. The role of F_{ovS} is more versatile in the CCM because when it is negative (positive) in the AMOC on state the model is in its multi-stable (monostable) regime.

Finally, the sea-ice processes are represented as follows and specifically for $\lambda^a = 3.5 \times 10^{-6} \text{ m s}^{-1}$. When the temperature for box n is lower than 5°C (its reference temperature), we assume that the sea-ice fraction of box n (f_n) grows linearly by 20% per degree cooling (Figure A2a). This is an arbitrary choice for the sea-ice growth and we do not use the freezing temperature for sea-ice growth as box n represents the volume-averaged temperature over the higher latitudes. To represent now the effect that sea ice suppress upper ocean mixing (Lin et al. 2023), we multiply the AMOC strength by a given AMOC reduction factor $0 \leq r_q \leq 1$ such that the AMOC strength becomes

$$q_N^{\text{ice}} = r_q q_N, \quad (4)$$

where q_N is the AMOC strength from (1). Since a continuous step-like change of the AMOC is found in the CESM (see Figure 4 in van Westen and Dijkstra (2023)), we use a similar function for the reduction factor (Figure A2b). We choose

$$r_q = \frac{1 - r_q^{\text{min}}}{2} \tanh(0.1 \times (0.5 - f_n)) + \frac{1 + r_q^{\text{min}}}{2}. \quad (5)$$

such that $r_q \sim 1$ when the sea-ice fraction $f_n < 0.4$ (40%) and, for $f_n > 0.6$ (60%), r_q decreases to a minimum value r_q^{min} . When $r_q = 1$ is chosen, the model does not represent any sea ice effects.

In the CESM results (van Westen and Dijkstra 2023), there is a factor 10 difference in spatially-averaged mixed layer depth over the Irminger basin between the two AMOC states (which would suggest $r_q^{\text{min}} \approx 0.1$) with local differences up to a factor 20 difference ($r_q^{\text{min}} \approx 0.05$). We will vary r_q^{min} below to investigate its sensitivity in the the E-CCM. Note that the value of r_q depends on the sea-ice fraction and hence on the temperature T_n , but sea ice is not dynamically resolved in the E-CCM and its effect is only parameterised.

c. Steady States and Transition Probabilities

To determine the bifurcation diagrams of the CCM and E-CCM we implemented the model equations in the continuation software AUTO-07p (Doedel et al. 2007, 2021). The AUTO software

is able to directly compute steady states versus model parameters without time integration by using a pseudo-arclength continuation combined with a Newton-Raphson method. An additional advantage of AUTO is its ability to detect special points such as Hopf and saddle-node bifurcations, which are both present in the CCM and E-CCM. The accuracy of AUTO is determined by three coefficients representing the absolute and relative accuracy of the solution, and the accuracy for locating special points. All these coefficients are set on a minimum value of 10^{-6} and a higher accuracy is used where necessary to determine an accurate bifurcation diagram.

In the multi-stable regime, we study noise-induced transitions in the stochastic version of the E-CCM. Stochastic variations in the asymmetric freshwater flux forcing are considered by adding a term $f_\sigma E_A S_0 \zeta(t)$ to the salinity equation of box n (and subtracting it from the salinity equation of box s), where $\zeta(t)$ is a zero mean, delta time correlated (white) noise process and f_σ controls the strength of the noise. Following Castellana et al. (2019), we use the Trajectory Adaptive Multilevel Splitting (TAMS) algorithm (Lestang et al. 2018) to determine probabilities of transitions between different steady AMOC states in the E-CCM within a given time interval T .

3. Results

a. Statistical Steady States in CESM

The branched simulations from the hysteresis experiment identify multiple statistical steady AMOC states in the CESM (Figure 2) for both $F_H = 0.18$ Sv and $F_H = 0.45$ Sv.

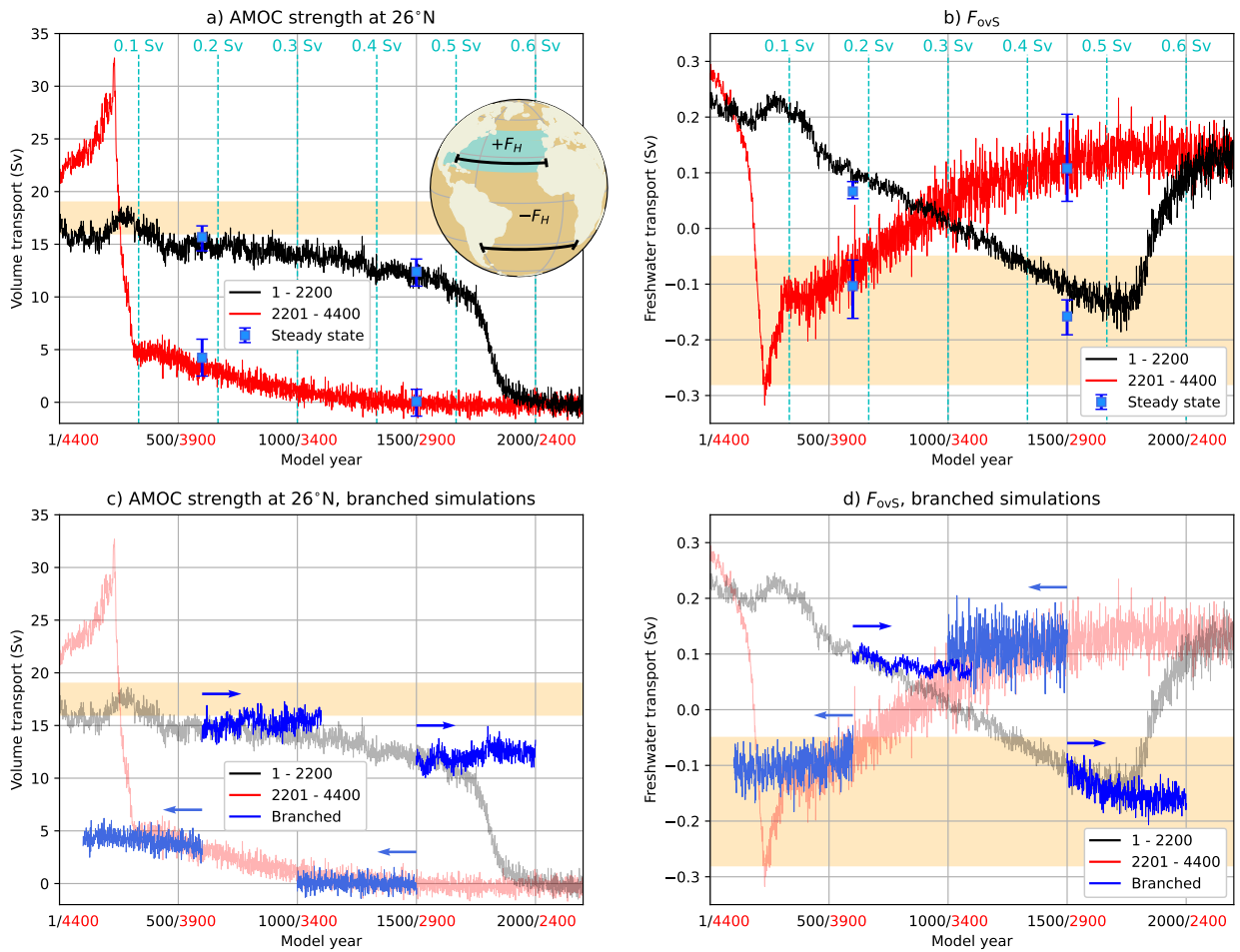
The first state is obtained from the strong northward overturning state for $F_H = 0.18$ Sv (branched from model year 600). The AMOC strength appears statistically stationary after 500 years of the branched simulation. When we consider the time means (450 – 500 years after the branching point), we find an AMOC strength and F_{ovS} of 15.7 Sv and 0.07 Sv, respectively. The results from the quasi-equilibrium simulation (model years 575 – 624) are close to the latter equilibrium values with 14.8 Sv for AMOC strength and 0.10 Sv for F_{ovS} . For $F_H = 0.18$ Sv (branched from model year 3,800), there is a second statistical steady state. This state has a weak and shallow (<1,000 m) northward overturning cell (van Westen and Dijkstra 2023) in the Atlantic Ocean with an equilibrium AMOC strength of 4.2 Sv and F_{ovS} of -0.10 Sv. The quasi-equilibrium values (model years 3,775 – 3,824) are 3.2 Sv and -0.07 Sv for the AMOC strength and F_{ovS} , respectively.

For $F_H = 0.45$ Sv (branched from model year 1,500), the AMOC is still in the northward overturning regime, but its strength has declined under the stronger freshwater forcing. The equilibrium values are 12.4 Sv for AMOC strength and -0.16 Sv for F_{ovS} , while the quasi-equilibrium approach (model years 1,475 – 1,524) values are 11.9 Sv and -0.10 Sv, respectively. As discussed in van Westen et al. (2024), the sign and variance in F_{ovS} are good indicators of the approach of the AMOC tipping point. The F_{ovS} variance for $F_H = 0.45$ Sv (2.1×10^{-4} Sv²) is indeed larger than at $F_H = 0.18$ Sv (0.33×10^{-4} Sv²), which is directly visible from the branched time series (Figure 2d). A linear trend was removed before determining the variances. The larger variance indicates that the AMOC loses resilience and is closer to its tipping point. The variances in AMOC strength are quite similar for both branches and are about 0.3 Sv². For $F_H = 0.45$ Sv another statistical steady state exists; this is the collapsed AMOC state (branched from model year 2,900). This equilibrium state has an AMOC strength of 0.08 Sv and F_{ovS} of 0.11 Sv and the values for the quasi-equilibrium approach (model years 2,875 – 2,924) are close to the equilibrium values.

The quasi-equilibrium simulation remains reasonably close to the steady states but also indicates that the freshwater forcing changes are faster than oceanic adjustment time scales. Ideally one would like to change the freshwater forcing even slower (than 3×10^{-4} Sv yr⁻¹) and determine more steady states, preferably closer to the tipping points, but these simulations require even more computational resources and are at the moment not feasible. As argued in van Westen and Dijkstra (2023), one would expect the AMOC recovery to occur at the value of F_H where F_{ovS} changes sign on the AMOC on branch (black curve in Figure 2b), that is around year 3,400 in the quasi-equilibrium approach. The results in Figure 2 show instead that a statistical steady AMOC off state still exists for $F_H = 0.18$ Sv and hence the late recovery at year 4,100 is not due to an overshoot but to the fact that, in a model with sea ice, AMOC off states can apparently extend to positive values of F_{ovS} . We will explore this below in more detail using the conceptual model.

b. Steady States in the E-CCM

To investigate the important role of sea ice in the AMOC hysteresis, we compute steady states in the deterministic E-CCM. First we analyse the case without sea ice (by setting $r_q^{\text{min}} = 1$) and vary the asymmetric freshwater flux forcing (E_A). The bifurcation diagrams for this case are shown



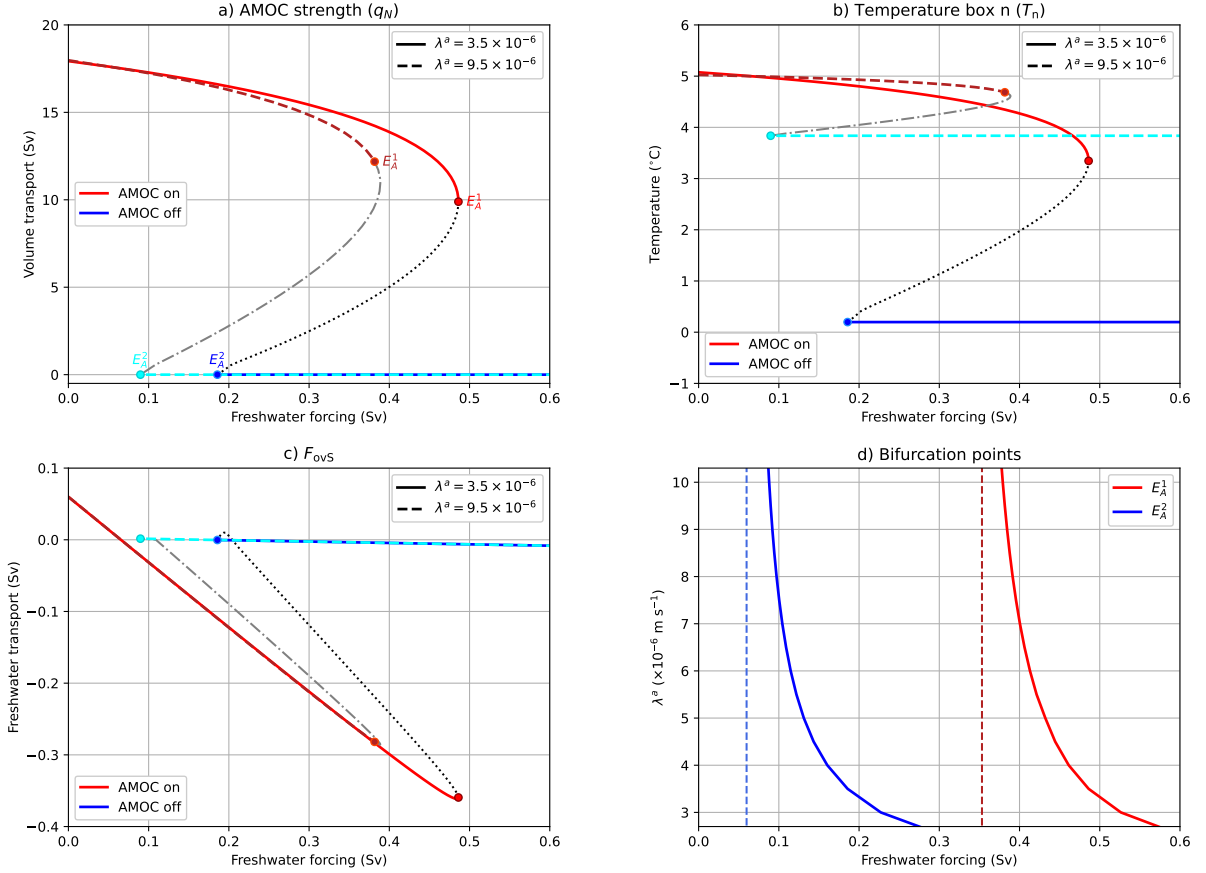
6 FIG. 2. (a): The AMOC strength at 1,000 m and 26°N . The cyan-coloured lines in panels a and b indicate
7 the magnitude of the freshwater forcing F_H and the yellow shading in all panels indicates observed ranges for
8 the presented quantity (Garzoli et al. 2013; Mecking et al. 2017; Smeed et al. 2018; Worthington et al. 2021).
9 The statistical equilibria (i.e., steady states in blue, panels a and b) of model years 600, 1,500, 2,900 and 3,800
10 are also shown, where the marker indicates the mean and the error bars show the minimum and maximum over
11 the last 50 years of the 600-year long branched simulations. Inset: The hosing experiment where fresh water
12 is added to the ocean surface between $20^\circ\text{N} - 50^\circ\text{N}$ in the Atlantic Ocean ($+F_H$) and is compensated over the
13 remaining ocean surface ($-F_H$). The black sections indicate the 26°N and 34°S latitudes over which the AMOC
14 strength and F_{ovS} are determined, respectively. (b): The freshwater transport by the AMOC at 34°S , F_{ovS} . (c
15 & d): Similar to panels a,b, but now the entire branched simulations are displayed. The arrows indicate the
16 beginning of the branches and the direction of time for each branch.

in Figure 3a for two values of λ^a . Both bifurcation points are saddle node bifurcations, similar to the CCM, and close to the saddle node bifurcations ($\Delta E_A = 0.002$ Sv) there are (subcritical) Hopf bifurcations which give unstable periodic orbits (not shown). The position of the bifurcation points is dependent on the heat exchange rate λ^a with the atmosphere and lower values of λ^a

(less restoring) result in a larger value of E_A at the saddle-node bifurcation points. In the limit of $\lambda^a \rightarrow \infty$, we find the same bifurcation points as in the CCM (dashed lines in Figure 3d). The hysteresis width, that is the distance between E_A^1 and E_A^2 , is about 0.3 Sv and does not depend much on λ^a .

To understand this behaviour of the shift of E_A^1 with λ^a , we analyse the AMOC strength response under varying E_A . The AMOC strength is represented by q_N and is proportional to the density difference between box n and box ts ($\Delta\rho$), and, given the linear equation of state, it boils down to $\Delta\rho \sim \Delta T - \Delta S$. Under the increasing freshwater forcing the salinity difference becomes larger and this decreases the density difference resulting in AMOC weakening (Figure 3a). The temperature of box n (T_n , Figure 3b) decreases as this box receives less heat from box t under AMOC weakening, which enhances the temperature difference between box n and box ts (the temperature of box ts remains fairly constant). This larger temperature difference between box n and box ts increases the density difference, so there are two counteracting effects that control the density difference. The combined effect of the temperature and salinity responses under the freshwater forcing shifts the saddle-node bifurcation point (E_A^1 , Figure 3d) to higher values of freshwater forcing when comparing this to the standard CCM (dashed lines in Figure 3d). The stabilising temperature effect is larger at smaller λ^a (less restoring) and hence a larger value of E_A^1 is needed to destabilise the AMOC (Figure 3) at the saddle-node bifurcation.

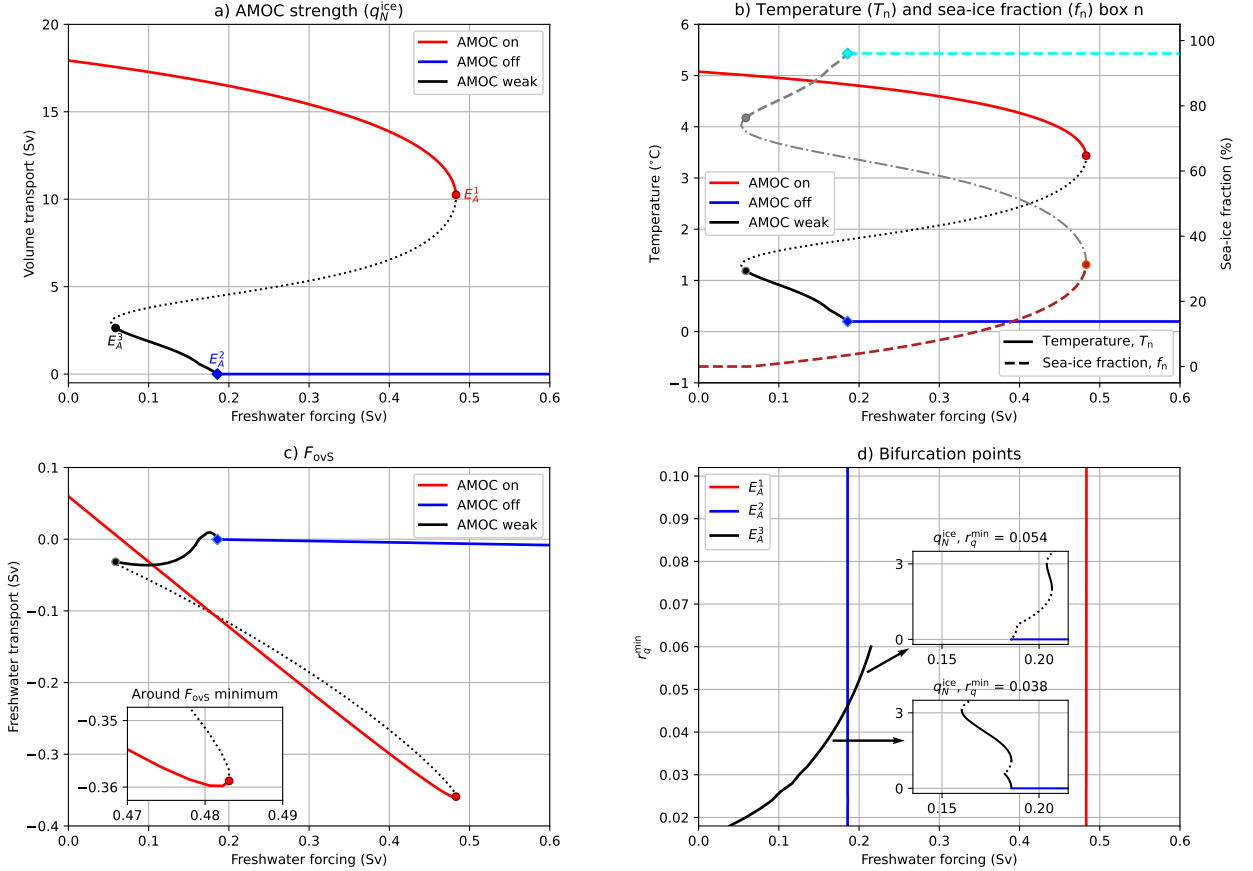
When the AMOC collapses, both temperature and salinity (strongly) decline in box n, these changes are much smaller for box ts. The density gradient is influenced by both salinity and temperature, the temperature response partly compensates the salinity response and hence the bifurcation point (E_A^2 , Figure 3d) also shifts to higher values of E_A compared to that of the CCM. Note that the temperature of box n does not vary much under the varying freshwater forcing when AMOC is in its off state (Figure 3b). This box is in equilibrium as it only receives heat from its overhead atmosphere and from the gyre transport with box t. The Hopf bifurcations near E_A^1 and E_A^2 have associated periods of about 60 to 200 years and 3,000 to 6,000 years, respectively. For relatively large values of λ^a , the value of E_A where F_{ovS} changes sign on the AMOC on branch is close to E_A^2 , similar as in the CCM. But for small values of λ^a (e.g., $\lambda^a = 3.5 \times 10^{-6} \text{ m s}^{-1}$), this is clearly not the case. In other words, negative F_{ovS} does not exclusively indicate the multi-stable regime.



17 FIG. 3. (a – c): The steady state solutions for the E-CCM (no sea ice) for the (a): AMOC strength, (b):
 18 temperature of box n and (c): F_{OVS} . The red and blue curves indicate the steady AMOC on and AMOC off state,
 19 respectively, and for two different values for λ^a (solid and dashed lines). The (dash)dotted curves are the unstable
 20 branches and the saddle-node bifurcation points are indicated by the circled markers. (d): The bifurcation points
 21 as a function of freshwater forcing for varying λ^a , the dashed lines indicate the bifurcation points for the CCM.

Next, the case with sea-ice representation in the E-CCM is considered for $\lambda^a = 3.5 \times 10^{-6} \text{ m s}^{-1}$. Figure 4 shows the bifurcation diagram for $r_q^{\min} = 0.02$, where the saddle node bifurcation E_A^2 in Figure 3 has moved to E_A^3 . The saddle-node E_A^1 is hardly affected as the AMOC reduction factor r_q is about 1 (relatively low sea-ice fractions when $f_n < 35\%$) when in the AMOC on state. At the value E_A^2 there is no longer a saddle-node bifurcation, but it remains an important point as q_N switches sign here; in the case without sea ice this would then result in AMOC recovery. However, in the presence of sea ice, the AMOC reduction factor is very strong (here $r_q \approx 0.02$) and a new branch of equilibrium states appears in which the AMOC remains weak (less than 3 Sv). For

decreasing values of the freshwater forcing, the AMOC becomes stronger and the sea-ice fraction starts declining until the AMOC reaches about 3 Sv at the new bifurcation point E_A^3 . There are again (subcritical) Hopf bifurcations close to the saddle nodes E_A^1 and E_A^3 with associated periods of 50 to 250 years and 200 to 1,250 years, respectively.



22 FIG. 4. (a – c): The steady state solutions for the E-CCM for the (a): AMOC strength, (b): temperature of box n
 23 and sea-ice fractions and (c): F_{ovS} . The red, blue and black curves indicate the AMOC on, AMOC off and AMOC
 24 weak state, respectively, for $\lambda^a = 3.5 \times 10^{-6} \text{ m s}^{-1}$ and $r_q^{\min} = 0.02$. The (dash)dotted curves are the unstable
 25 branches and the saddle-node bifurcation points are indicated by the circled markers, the diamond marker is not
 26 a saddle-node bifurcation point. The inset in panel c is a zoom in around the F_{ovS} minimum of the AMOC on
 27 branch. (d): The bifurcation points as a function of E_A for varying r_q^{\min} and for $\lambda^a = 3.5 \times 10^{-6} \text{ m s}^{-1}$. The
 28 two insets shows the steady state for AMOC strength (q_N^{ice} , similar to panel a) for $r_q^{\min} = 0.038$ and $r_q^{\min} = 0.054$,
 29 centred around the weak state.

When decreasing the freshwater forcing from E_A^2 , F_{ovS} becomes slightly positive and then changes sign. In this freshwater forcing range, the AMOC strength is very weak ($q_N^{\text{ice}} < 0.6$ Sv) and q_S remains negative. Lowering the freshwater forcing further results in a stronger AMOC and q_S becomes positive, which induces a negative F_{ovS} . In the CCM, negative values of F_{ovS} in the AMOC on state mark the multi-equilibrium regime (Castellana et al. 2019) and here for $r_q^{\text{min}} = 0.02$ this is (by coincidence) also the case (Figure 4c). However, for $r_q^{\text{min}} < 0.02$ the bifurcation point E_A^3 shifts to lower values of the freshwater forcing and then positive F_{ovS} are in multi-equilibrium regime, similar as in the CESM. The quantity F_{ovS} is still an important indicator in the CESM as its sign change coincides with the initial AMOC recovery but the AMOC strength is strongly suppressed by sea-ice processes (van Westen and Dijkstra 2023). When using a larger λ^a and a different sea-ice response function in the E-CCM, we can tune the model such that E_A^2 is close the F_{ovS} sign change, similar as in the CESM.

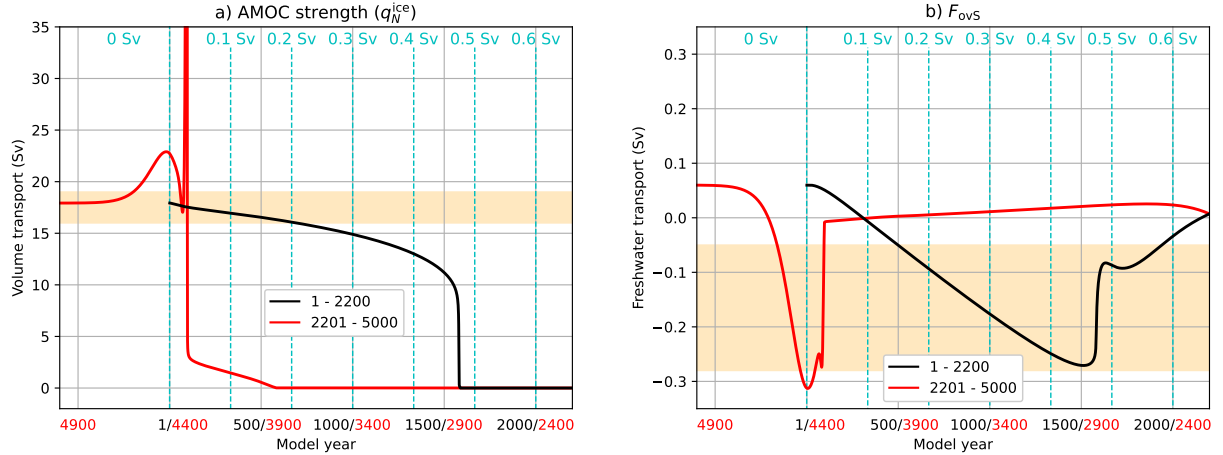
It is interesting that the weak state splits into two sub-branches for $0.030 \leq r_q^{\text{min}} \leq 0.052$ (inset in Figure 4d for $r_q^{\text{min}} = 0.038$); the AMOC on and AMOC off states remain very similar. The two sub-branches differ in F_{ovS} sign and there are subcritical Hopf bifurcations near three saddle-node bifurcations located on E_A^1 , E_A^2 , and E_A^3 . The associated periods for the Hopf bifurcations near E_A^1 and E_A^3 are 50 – 500 years and 150 – 500 years, respectively. The Hopf bifurcation near E_A^2 has a much longer associated period of 44,000 – 52,000 years. For $0.052 < r_q^{\text{min}} \leq 0.060$ only the weak state with negative F_{ovS} remains (inset in Figure 4d for $r_q^{\text{min}} = 0.054$) and E_A^2 is now a saddle node (similar to Figure 3). For increasing r_q^{min} , the saddle node E_A^3 shifts to larger values of E_A and has a maximum AMOC strength of 3 Sv. The AMOC weak state only appears when the AMOC reduction factor is sufficiently low ($r_q^{\text{min}} \leq 0.060$) and for very low values of this factor ($r_q^{\text{min}} < 0.015$) a negative freshwater forcing is required to return to the AMOC on state (Figure 4d). Note that for $r_q^{\text{min}} > 0.060$ the bifurcation point E_A^3 disappears and then the results are similar to Figure 3. The hysteresis width also varies for varying r_q^{min} . For values of $r_q^{\text{min}} \geq 0.046$, it is a constant width of 0.3 Sv while the hysteresis width increases for lower values for r_q^{min} . For example, for $r_q^{\text{min}} = 0.02$ it is about 0.4 Sv which is comparable to that of the CESM.

c. Quasi-equilibrium Experiment in the E-CCM

When varying the freshwater flux forcing over time with a rate of 3×10^{-4} Sv yr⁻¹ (similar to the CESM), we find qualitatively the same hysteresis behaviour in the E-CCM (Figure 5) as in the CESM (Figure 2). Note that we continued the simulation beyond model year 4,400 under no freshwater forcing to run the model into equilibrium. We find an AMOC tipping event around model year 1,600 and F_{ovS} goes through a minimum and further equilibrates to the reversed circulation. The steady states show the F_{ovS} minimum prior to the AMOC tipping point (inset in Figure 4c) with a difference of only $\Delta E_A = 8 \times 10^{-4}$ Sv. Other idealised models find (qualitatively) a similar timing between F_{ovS} minimum and AMOC tipping (Dijkstra 2007; Huisman et al. 2010) and in the CESM (van Westen et al. 2024).

The AMOC remains in its off state until around model year 3,900 and q_N^{ice} becomes positive and F_{ovS} switches sign. Eventually the AMOC transitions to the on state and strongly overshoots (to 68 Sv). This overshoot is a model artefact as the AMOC strength is then determined by the (instantly felt) density difference between box n and box ts and by the pycnocline depth which is about twice as deep. The AMOC in the CESM is not only controlled by this density difference and the pycnocline depth, which explains why the CESM does not have such a large overshoot. There is a second overshoot in AMOC strength of about 22.9 Sv (around model year 4,400), which is more realistic and dynamically driven. Advection of temperature and salinity controls the adjustment time scale from the weak AMOC to the AMOC on state and this takes about a few centuries, which is much faster than in the CESM (or real ocean), where vertical mixing also plays an important role. Nevertheless, prior to the full adjustment to the AMOC on state, the different temperature and salinity gradients (w.r.t. the initial state) allow for a temporarily stronger AMOC strength. At the same time, F_{ovS} reaches its minimum and then switches sign when the salinity in the boxes further adjust to the AMOC on state.

The transient responses in the E-CCM are comparable to that of the CESM. The deviations in the quasi-equilibrium approach w.r.t. the steady states of the AMOC on branch become larger when approaching the tipping point. Note that the timing of AMOC collapse and recovery is not identical to that of the CESM, it is possible to vary the λ^a and the AMOC reduction and sea-ice response functions to tune the E-CCM even better to the CESM results. The important result here is that the



30 FIG. 5. (a): The AMOC strength (q_N^{ice}) and (b): the freshwater transport by the AMOC at 30°S in the E-CCM
 31 for $\lambda^a = 3.5 \times 10^{-6} \text{ m s}^{-1}$ and $r_q^{\text{min}} = 0.02$. The cyan-coloured lines in panels a and b indicate the magnitude of
 32 E_A . The yellow shading in all panels indicates observed ranges for AMOC strength and F_{ovS} . Note that after
 33 model year 4,400 the freshwater forcing is held constant at $E_A = 0 \text{ Sv}$.

E-CCM reasonably captures the AMOC responses from the CESM with only a few adjustment to the original model.

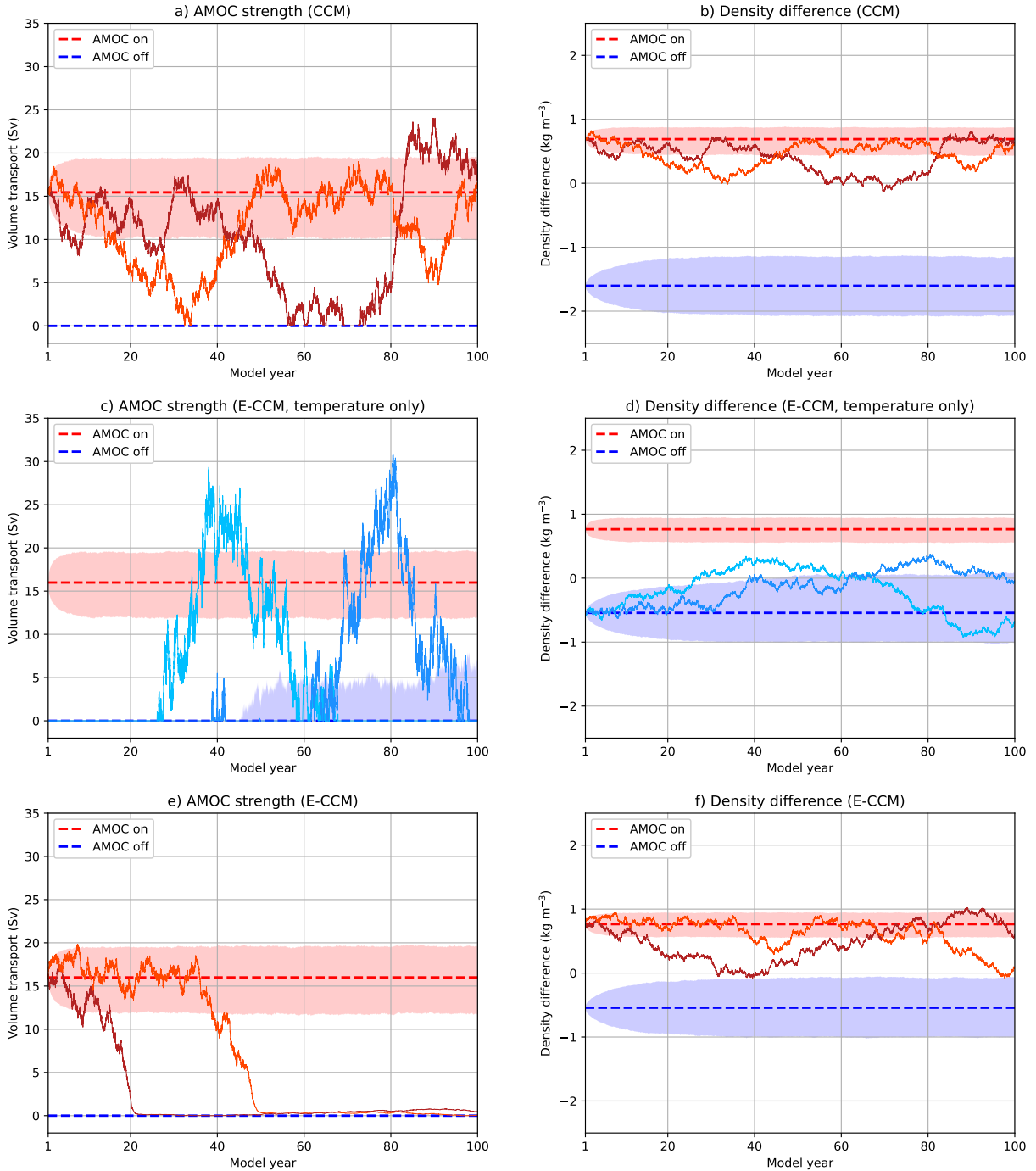
d. Transition Probabilities in the E-CCM

We define an on-to-off transition as a transition from the steady AMOC on state to an AMOC state which strength is below a certain threshold (here taken as 0 Sv for the no sea-ice case and 1 Sv for the sea-ice case). In addition, an off-to-on transition is a transition from the steady AMOC off state to an AMOC which strength is larger or equal to the strength of the steady AMOC on state. We repeat the TAMS procedure (Lestang et al. 2018) 15 times and then determine the mean transition probability p (and its standard deviation) of specific transitions within $T = 100$ years, similar to Castellana et al. (2019). Given this relatively short time interval (w.r.t. the dynamics of the E-CCM) we only find typical F-type (fast) transitions (Castellana et al. 2019). Full collapses (i.e., AMOC on \rightarrow AMOC collapsed) or full recoveries (i.e., AMOC collapsed \rightarrow AMOC on), i.e. S-type transitions (Castellana et al. 2019), take much longer time intervals (a few centuries) and are not considered.

The CCM forced by freshwater noise ($f_\sigma = 0.085$) for $E_A = 0.25$ Sv undergoes an on-to-off transition and then quickly returns to its AMOC on state (Figures 6a). These AMOC transitions are reflected in the sign change of the density difference between box n and box ts (Figures 6b). The AMOC state is controlled by the sign in density difference and its magnitude determines the transition probability. The magnitude of this density difference is larger in the steady AMOC off state (-1.6 kg m^{-3}) than the steady AMOC on state ($+0.7 \text{ kg m}^{-3}$) and the larger the difference in absolute magnitude the lower the transition probabilities (Figures 7a,b). In other words, realisations with large density differences require relatively large freshwater noise perturbation to make a transition. The transition probability under this freshwater noise forcing is $p < 10^{-9}$ for off-to-on transitions and is substantially lower than for on-to-off transitions ($p = 0.0025 \pm 0.0001$). This much lower transition probability also explains why there are no off-to-on transitions for this particular noise realisation as more than 10^9 noise realisations are required to expect at least 1 transition, whereas we used only 5,000 realisations in Figures 6a,b. Lowering the freshwater forcing towards the second bifurcation point ($E_A^2 \approx 0.06$ Sv) would favour off-to-on transitions while on the other hand the probability of on-to-off transitions decreases (Figures 7c).

Under the same freshwater noise forcing for the E-CCM ($r_q = 1$ (no sea-ice effects), $\lambda^a = 3.5 \times 10^{-6} \text{ m s}^{-1}$), we mainly find off-to-on transitions (Figures 6c,d). In this set-up the system is much closer to its second bifurcation point E_A^2 ; this is also reflected in the smaller (absolute) density difference in the AMOC off state (-0.5 kg m^{-3}) than in the AMOC on state ($+0.8 \text{ kg m}^{-3}$). Under these freshwater noise forcing, the transition probabilities are $p = 7.9 \times 10^{-7} \pm 0.9 \times 10^{-7}$ (on-to-off transitions) and $p = 0.064 \pm 0.002$ (off-to-on transitions). The overall transition probabilities in the E-CCM with no sea-ice effects (Figures 7d,e,f) are higher than in the CCM (Figures 7a,b,c) when using the distance to the bifurcation points as a reference for both model configurations. This is because the magnitude of the freshwater noise forcing is given by $f_\sigma E_A$ and, as the bifurcation points are shifted to higher values of E_A (Figure 3d) when temperature is included, it results in a larger freshwater noise forcing allowing for higher transition probabilities.

The density differences remain unaltered ($< 0.001\%$ difference w.r.t. $r_q = 1$) when including sea ice ($r_q^{\min} = 0.02$) in the E-CCM. Yet, there are now on-to-off transitions (Figures 6e,f). The density difference of the two (random) realisations remains positive after an AMOC collapse and the AMOC reduction factor (in the presence of sufficient sea ice) is strong enough to limit their

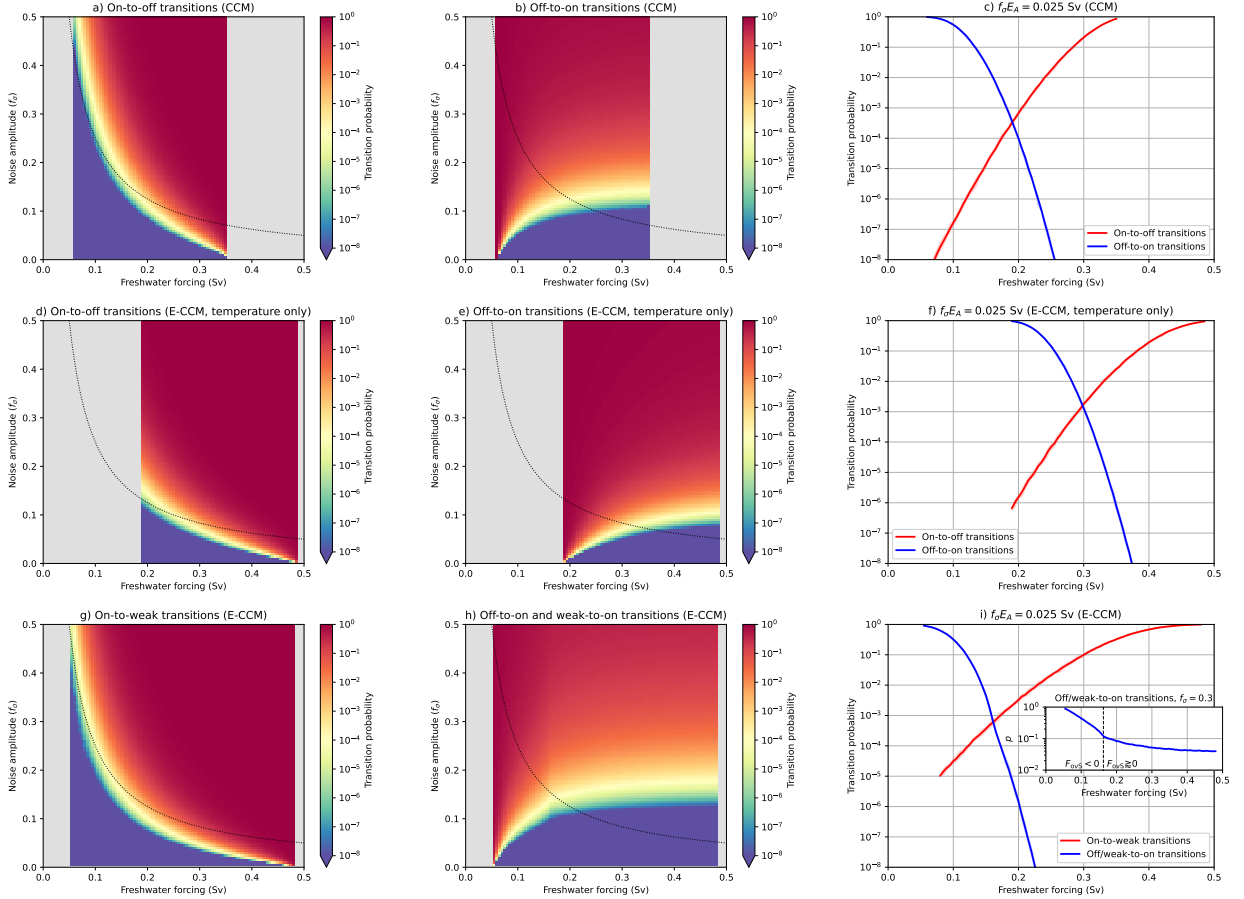


34 FIG. 6. Transitions in the (E-)CCM for $f_{\sigma} = 0.085$ and $E_A = 0.25$ Sv for the AMOC strength (left column)
 35 and density difference between box n and box ts (right column). The dashed lines indicate the statistical steady
 36 AMOC on (red) and the AMOC off (blue) statistical steady state, where the shading indicates the 95%-confidence
 37 level derived from 5,000 different noise realisations (for each statistical steady state). A few random realisations
 38 are displayed which (temporarily) undergo an on-to-off transition (red curves) or an off-to-on transition (blue
 39 curves).

AMOC strength to almost 0 Sv. On relatively short time scales (< 100 years) the system undergoes an F-type transition and remains in a weak AMOC state (i.e., AMOC strength slightly larger than 0 Sv). Note that this state is unstable for the imposed freshwater forcing conditions and when the system further equilibrates, it makes the full transition to the stable AMOC collapsed state. These transitions are somewhat different compared to the other two model set-ups and we define on-to-off transitions when $q_N^{\text{ice}} < 1$ Sv, and we label them as on-to-weak transitions for the E-CCM. Sea ice suppresses the AMOC strength and this strongly limits off-to-on transitions ($p < 10^{-9}$) compared to on-to-weak transitions ($p = 0.0031 \pm 0.0003$) under $f_\sigma = 0.085$ and $E_A = 0.25$ Sv. The much lower transition probabilities (Figures 7g,h,i) compared to the other model set-ups clearly show that the AMOC weak/off state is much more resilient than the AMOC on state. On the other hand, the on-to-weak transitions are more likely when including sea ice (compare red curves in Figures 7f and 7i for $E_A^2 < E_A < E_A^1$) and this indicates that sea-ice processes destabilise the AMOC on state.

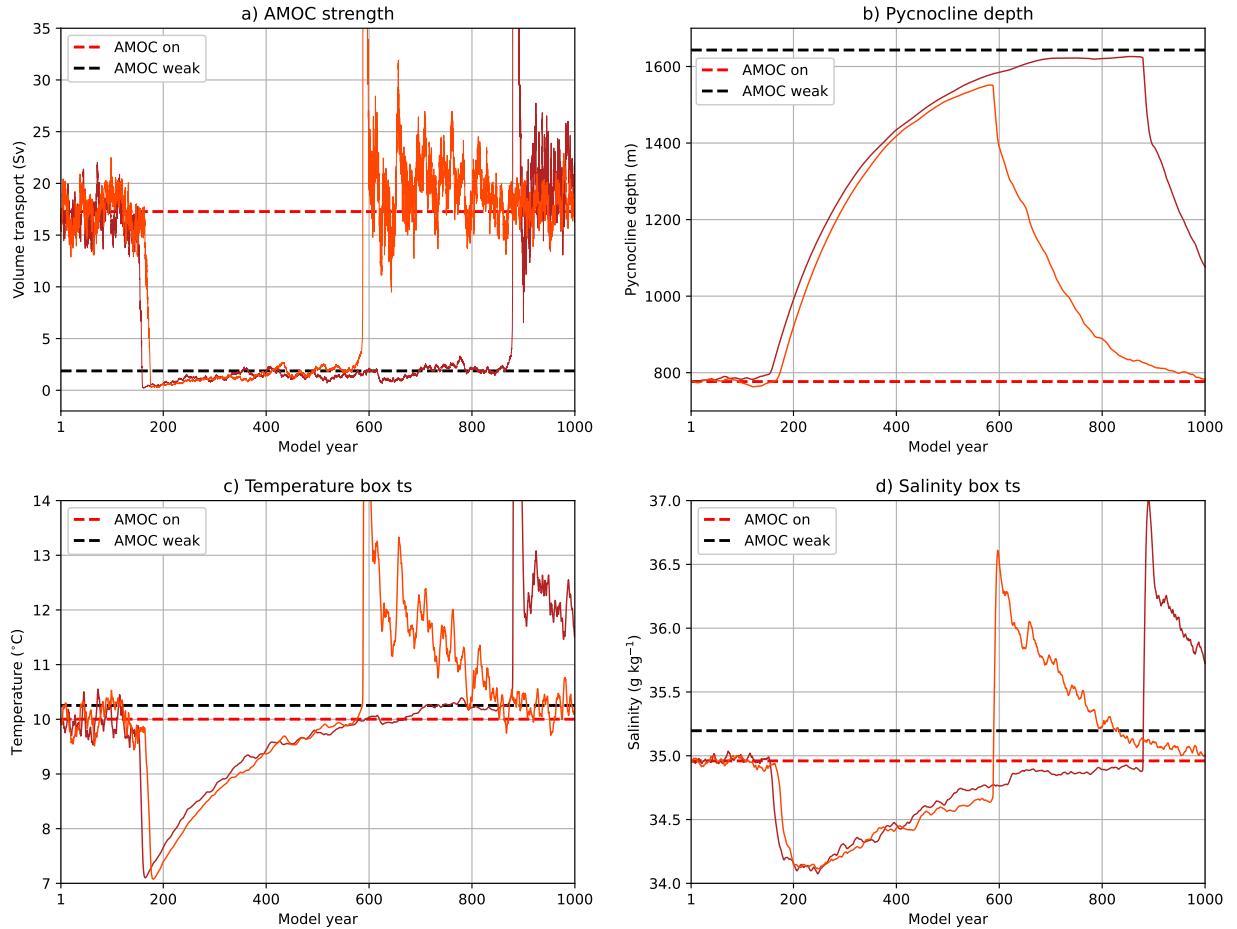
For $r_q^{\text{min}} = 0.02$ one stable AMOC weak state exists and this state has both positive and negative F_{ovS} values (Figure 4). Salinity perturbations are amplified under negative F_{ovS} (i.e., the salt-advection feedback) and this part of the AMOC weak state is relatively unstable compared to the part with positive F_{ovS} . The quantity $\phi = \left| \frac{\partial \log p}{\partial E_A} \right|$ is indeed larger for $F_{\text{ovS}} < 0$ (inset in Figure 7i) and for varying f_σ , indicating that the salt-advection feedback destabilises this part of the weak state where $F_{\text{ovS}} < 0$ and resulting in higher transition probabilities.

Once the E-CCM undergoes an on-to-weak transition, it is also possible to return back to the original AMOC on state. Figure 8 shows two realisations which undergo such behaviour for $f_\sigma = 0.25$ and $E_A = 0.10$ Sv. Note that we simulate the trajectories for 1,000 years in Figure 8 because the model trajectory first needs to equilibrate to the AMOC weak state before the second transition is possible. The strong transient responses in the pycnocline and temperature and salinity for box ts dominate the dynamics of the system as the AMOC strength is (partly) dependent on these oceanic properties. The strong decline in the temperature and salinity (around model year 200) is related to the deepening of the pycnocline, resulting in a volume expansion of box ts and hence lowering of these quantities. The temperature and salinity in box n (not shown) also decrease under an AMOC collapse and remain fairly constant from model year 200 until AMOC recovery. Once the model trajectory is sufficiently adjusted to the stable AMOC weak state (about 400 years after collapse), it may undergo again random transitions to the AMOC on state. The transition



40 FIG. 7. Mean transition probabilities (within 100 years) in the (E-)CCM for varying f_σ and E_A , with Δf_σ
 41 = 0.005 and $\Delta E_A = 0.005$ Sv. The on-to-off (or on-to-weak) transitions are shown in the left column and the
 42 off/(weak)-to-on transitions in the middle column. For the regions shaded in gray only one AMOC steady state
 43 exists. The dotted curve indicates the freshwater noise forcing of 0.025 Sv ($= f_\sigma E_A$) and the mean transition
 44 probabilities along this freshwater noise forcing are shown in the right column, the shading indicates the minimum
 45 and maximum transition probabilities derived from 15 independent TAMS realisations. The inset in panel i shows
 46 the mean transition probabilities for the E-CCM for $f_\sigma = 0.3$ under varying E_A , and only for off/weak-to-on
 47 transitions.

probabilities from Figure 7 cannot (directly) be used to determine the transition probability of undergoing two consecutive transitions due to the setup of TAMS using fixed score functions (Castellana et al. 2019).



48 FIG. 8. Two random realisations undergoing transitions in the E-CCM ($\lambda^a = 3.5 \times 10^{-6} \text{ m s}^{-1}$ and $r_q^{\min} = 0.02$)
 49 for $f_\sigma = 0.25$ and $E_A = 0.10 \text{ Sv}$ for various quantities. The dashed lines indicate the steady AMOC on (red) and
 50 AMOC weak (black) states for each presented quantity.

4. Summary and Discussion

In this study we analysed AMOC hysteresis behaviour in the CESM (van Westen and Dijkstra 2023) and branched off four additional simulations under constant freshwater forcing to determine statistical steady states. We found three different statistical steady states in the CESM: the AMOC on state, the AMOC off state and the AMOC weak state. Sea-ice processes strongly influence the AMOC strength and modify the AMOC hysteresis (van Westen and Dijkstra 2023), giving rise to the AMOC weak state. This stable AMOC weak state is not found in ocean-only models in which sea-ice processes are not resolved (Dijkstra 2007; Huisman et al. 2010). The existence of a broad

multi-stable regime under varying freshwater forcing suggests that noise-induced AMOC tipping is possible in the CESM. However, we can not yet determine these transition probabilities for the CESM due to computational limitations.

To determine the effects of the sea-ice processes on the AMOC transition probabilities, we developed a novel stochastic ocean-sea-ice box model (the E-CCM). The original 5-box model (Cimatoribus et al. 2014; Castellana et al. 2019) was extended by dynamically solving for temperatures and parameterising the effects of sea ice on the AMOC. When the effects of sea ice are strong enough to suppress the AMOC strength, it modifies the AMOC hysteresis and gives rise to the AMOC weak state. The deterministic box model can qualitatively reproduce the CESM hysteresis behaviour, which is again an example of the usefulness of conceptual models to understand AMOC dynamics (Dijkstra 2023). The existence of this weak state also illustrates the crucial importance of sea-ice processes on the AMOC strength (van Westen and Dijkstra 2023). This is in agreement with the results in Lin et al. (2023), who show in CMIP6 models that sea-ice effects play a major role (through their effect on the Labrador Sea stratification) in the decline of the AMOC under increased greenhouse gas concentrations.

The sea-ice parametrisation in the E-CCM only affects the AMOC strength and does not consider brine rejection nor thermodynamics. Despite these shortcomings, Hopf bifurcations exist in the E-CCM and this is consistent with earlier works (Yang and Neelin 1993; Broecker et al. 1990) where realistic sea-ice AMOC interactions have been studied to understand natural AMOC variability. Sea ice also plays an important role in Dansgaard-Oeschger events (Peltier and Vettoretti 2014; Vettoretti and Peltier 2016; Boers et al. 2018) and the recent AMOC hysteresis experiment conducted with the CESM confirms this (van Westen and Dijkstra 2023). Biases in the North Atlantic sea-ice distribution influence the background AMOC strength and the transient AMOC responses due to climate change (Lin et al. 2023) and can lead to rate-induced tipping (Lohmann and Ditlevsen 2021). These studies and the results presented here suggest a prominent role for sea-ice processes in AMOC dynamics and variability.

The stochastic E-CCM enables to compute the transition probabilities between the different AMOC states under freshwater noise forcing using rare-event algorithms (i.e., TAMS, Lestang et al. (2018)). The presence of sea ice increases the probability of on-to-off and on-to-weak transitions and sea ice strongly reduces the probability of weak-to-on and off-to-on transitions

of the AMOC. This indicates that the AMOC off and weak states, which are both influenced by sea ice, are much more stable than the AMOC on state. Although the quantitative results will be sensitive to the parameterisation of sea ice and its effects on the AMOC in the E-CCM, they provide meaningful insights into the effects of sea-ice processes in the AMOC hysteresis behaviour and AMOC transition probabilities.

An interesting follow-up study is to analyse the AMOC transition behaviour, and in particular the role of sea ice, under climate change. The suppressing effects of sea ice on the AMOC become smaller as sea ice is less likely to form under higher temperatures. As the AMOC weak state is strongly controlled by sea ice, this state would (partly) disappear. This stabilises the AMOC as transition probabilities from the AMOC on to AMOC weak state cease to exist over an interval of freshwater forcing. On the other hand, climate change also induces different temperature gradients which may destabilise the AMOC. A combination of E-CCM analyses together with targeted CESM simulations can be very useful for such a follow-up study.

Acknowledgments. We thank Michael Kliphuis (IMAU, UU) for performing the additional CESM simulations. The model simulations and the analysis of all the model output was conducted on the Dutch National Supercomputer (Snellius) within NWO-SURF project 17239. R.M.v.W., A.A.B. and H.A.D. are funded by the European Research Council through the ERC-AdG project TAOC (PI: Dijkstra, project 101055096). V.J.D. is funded by the European Union’s Horizon 2020 research and innovation programme CriticalEarth under the Marie Skłodowska-Curie grant agreement (project 956170). The authors declare no conflict of interest.

Data availability statement. The Python codes for the E-CCM can be accessed through <https://doi.org/10.5281/zenodo.10554659>, together with the CESM model output.

APPENDIX

Supporting Information on the Idealised Model Simulations

The CCM consists of five equations for salinity (four dynamical and one to conserve salinity) and one equation for the pycnocline. The equations are repeated here but we refer to Castellana et al. (2019) where all the different terms are explained (θ is the Heaviside function) and input parameters are also provided:

$$\frac{d(V_t S_t)}{dt} = q_S (\theta(q_S) S_{ts} + \theta(-q_S) S_t) + q_U S_d - \theta(q_N) q_N S_t + r_S (S_{ts} - S_t) + r_N (S_n - S_t) + 2E_S S_0 \quad (\text{A1a})$$

$$\frac{d(V_{ts} S_{ts})}{dt} = q_{Ek} S_s - q_e S_{ts} - q_S (\theta(q_S) S_{ts} + \theta(-q_S) S_t) + r_S (S_t - S_{ts}) \quad (\text{A1b})$$

$$\frac{d(V_n S_n)}{dt} = \theta(q_N) q_N (S_t - S_n) + r_N (S_t - S_n) - (E_S + E_A) S_0 \quad (\text{A1c})$$

$$\frac{d(V_s S_s)}{dt} = q_S (\theta(q_S) S_d + \theta(-q_S) S_s) + q_e S_{ts} - q_{Ek} S_s - (E_S - E_A) S_0 \quad (\text{A1d})$$

$$V_d S_d = S_0 V_0 - V_t S_t - V_{ts} S_{ts} - V_n S_n - V_s S_s \quad (\text{A1e})$$

$$\left(A + \frac{L_x A L_y}{2} \right) \frac{dD}{dt} = q_U + q_{Ek} - q_e - \theta(q_N) q_N \quad (\text{A1f})$$

The ocean heat content evolution equations (under the assumption of constant heat capacity and reference density) are fairly similar to the salinity ones and are given by:

$$\frac{d(V_t T_t)}{dt} = q_S (\theta(q_S) T_{ts} + \theta(-q_S) T_t) + q_U T_d - \theta(q_N) q_N T_t + r_S (T_{ts} - T_t) + r_N (T_n - T_t) - \lambda^a A_t (T_t - T_t^a) \quad (\text{A2a})$$

$$\frac{d(V_{ts} T_{ts})}{dt} = q_{Ek} T_s - q_e T_{ts} - q_S (\theta(q_S) T_{ts} + \theta(-q_S) T_t) + r_S (T_t - T_{ts}) - \lambda^a A_{ts} (T_{ts} - T_{ts}^a) \quad (\text{A2b})$$

$$\frac{d(V_n T_n)}{dt} = \theta(q_N) q_N (T_t - T_n) + r_N (T_t - T_n) - \lambda^a A_n (T_n - T_n^a) \quad (\text{A2c})$$

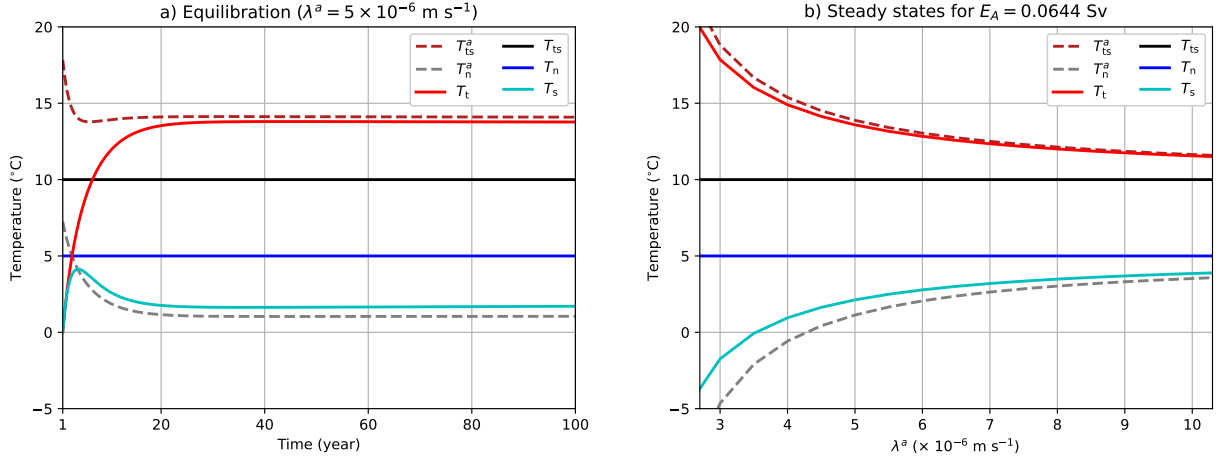
$$\frac{d(V_s T_s)}{dt} = q_S (\theta(q_S) T_d + \theta(-q_S) T_s) + q_e T_{ts} - q_{Ek} T_s - \lambda^a A_s (T_s - T_s^a) \quad (\text{A2d})$$

$$\frac{d(V_d T_d)}{dt} = \theta(q_N) q_N T_n - q_S (\theta(q_S) T_d + \theta(-q_S) T_s) - q_U T_d \quad (\text{A2e})$$

Using the standard input parameters from Castellana et al. (2019), we set the ocean surface areas to $3 \times 10^{13} \text{ m}^2$ (A_s), $1 \times 10^{13} \text{ m}^2$ (A_{ts}), $10 \times 10^{13} \text{ m}^2$ (A_t) and $1 \times 10^{13} \text{ m}^2$ (A_n). For more details how to integrate the model we refer to the publicly-available Python software.

To initialise the E-CCM, we use the steady state solution from the CCM for an arbitrary freshwater forcing E_A (here 0.0644 Sv) in the AMOC on state. The temperatures for box n and box ts are initialised at 5°C and 10°C (Castellana et al. 2019), respectively, and the temperatures for the other boxes can be arbitrarily chosen (here 0°C). To remain at this steady state for the E-CCM, we solve for each time step the equations $\frac{d(V_{ts} T_{ts})}{dt} = 0$ and $\frac{d(V_n T_n)}{dt} = 0$ for T_{ts}^a and T_n^a , respectively. This guarantees that the temperatures for box ts and box n remain the same over the entire simulation and hence we remain at the same steady state as the one from Castellana et al. (2019). To reduce the degrees of freedom, we assume the same atmospheric temperatures for the tropical boxes ($T_t^a = T_{ts}^a$) and polar boxes ($T_s^a = T_n^a$). All the other temperatures are free to evolve and we quickly reach a steady state for a given λ^a (Figure A1a) and running the simulation further (2,000 years) does not change the steady states (Figure A1b). The steady states of the deep ocean temperature (not shown) are very close to T_n (T_s) in the AMOC on state (off state).

Box n receives relatively warm water from box t (in the AMOC on state), which has to be balanced by a colder overhead atmosphere so that box n remains at a constant temperature of 5°C . For box ts, it is the exact opposite, this box receives relatively cold water from box s (in the AMOC on state) and a warmer overhead atmosphere is needed to balance this (negative) heat transport from box s. The temperature of box s and box t are also influenced by the changing atmospheric temperatures (they

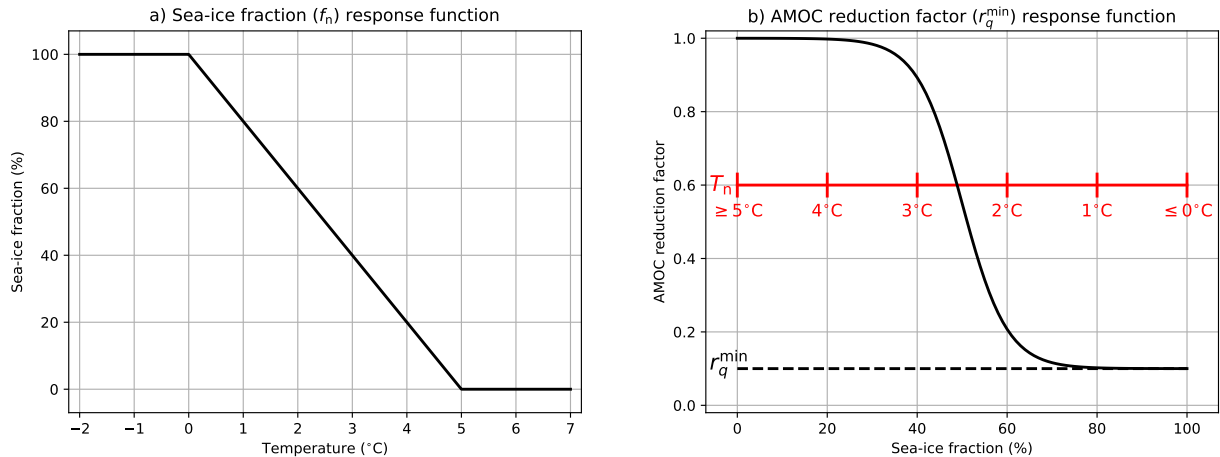


51 FIG. A1. (a): Evolution of the ocean (solid) and atmosphere (dashed) temperatures over the first 100 years
 52 for $\lambda^a = 5 \times 10^{-6} \text{ m s}^{-1}$, where $T_n = 5^{\circ}\text{C}$ and $T_{ts} = 10^{\circ}\text{C}$ are fixed. (b): The steady states (after 2,000 years of
 53 integration) temperatures for varying λ^a .

are coupled: $T_t^a = T_{ts}^a$ and $T_s^a = T_n^a$) and remain close to their overhead atmospheric temperatures. Decreasing λ^a to values below $3 \times 10^{-6} \text{ m s}^{-1}$ results in very cold (and unrealistic) atmospheric and oceanic temperatures (Figure A1b). In the limit of $\lambda^a \rightarrow \infty$, the atmospheric temperatures are 5°C (T_n^a) and 10°C (T_{ts}^a) and temperature anomalies in box n and box ts decay immediately, resulting in constant temperatures of 5°C and 10°C , respectively. This gives the same results as in the CCM. After determining the steady states for a given λ^a (Figure A1b), we fix the atmospheric temperatures and use those as input parameters for the E-CCM. All ocean temperatures are now free to evolve under a changing freshwater forcing E_A and the steady state is identical to the one from Castellana et al. (2019) for the reference E_A value (here 0.0644 Sv).

References

- Armstrong McKay, D. I., and Coauthors, 2022: Exceeding 1.5 C global warming could trigger multiple climate tipping points. *Science*, **377** (6611), eabn7950.
- Ashwin, P., S. Wieczorek, R. Vitolo, and P. Cox, 2012: Tipping points in open systems: bifurcation, noise-induced and rate-dependent examples in the climate system. *Philosophical Transactions of the Royal Society A*, **370**, 1166–1184.



54 FIG. A2. (a): Sea-ice response function as a function of the temperature of box n. (b): The AMOC reduction
 55 factor as a function of the sea-ice fraction of box n for a given r_q^{\min} .

Baars, S., D. Castellana, F. Wubs, and H. Dijkstra, 2021: Application of adaptive multilevel splitting to high-dimensional dynamical systems. *Journal of Computational Physics*, **424**, 109–876, <https://doi.org/10.1016/j.jcp.2020.109876>, 2011.05745.

Baatsen, M., A. S. Von Der Heydt, M. Huber, M. A. Klijhuis, P. K. Bijl, A. Sluijs, and H. A. Dijkstra, 2020: The middle to late Eocene greenhouse climate modelled using the CESM 1.0.5. *Climate of the Past*, **16** (6), 2573–2597.

Boers, N., 2021: Observation-based early-warning signals for a collapse of the Atlantic Meridional Overturning Circulation. *Nature Climate Change*, **11** (8), 680–688, <https://doi.org/10.1038/s41558-021-01097-4>.

Boers, N., M. Ghil, D. R. P. o. the, and 2018, 2018: Ocean circulation, ice shelf, and sea ice interactions explain Dansgaard–Oeschger cycles. *Proceedings National Acad Sciences*, <https://doi.org/10.1073/pnas.1802573115/-/dcsupplemental>.

Brocker, W., G. Bond, M. Klas, G. Bonani, and W. Wolfli, 1990: A salt oscillator in the glacial atlantic? 1. *The concept: Paleoceanography*, **5**, 469–477.

Caesar, L., G. D. McCarthy, D. Thornalley, N. Cahill, and S. Rahmstorf, 2021: Current Atlantic meridional overturning circulation weakest in last millennium. *Nature Geoscience*, **14** (3), 118–120.

- Caesar, L., S. Rahmstorf, A. Robinson, G. Feulner, and V. Saba, 2018: Observed fingerprint of a weakening Atlantic Ocean overturning circulation. *Nature*, **556 (7700)**, 191–196.
- Castellana, D., S. Baars, F. W. Wubs, and H. A. Dijkstra, 2019: Transition probabilities of noise-induced transitions of the Atlantic Ocean circulation. *Scientific Reports*, **9 (1)**, 20 284.
- Cessi, P., 1994: A simple box model of stochastically forced thermohaline flow. *Journal of Physical Oceanography*, **24**, 1911–1920.
- Cimatoribus, A. A., S. S. Drijfhout, and H. A. Dijkstra, 2014: Meridional overturning circulation: Stability and ocean feedbacks in a box model. *Climate dynamics*, **42**, 311–328.
- Dijkstra, H. A., 2007: Characterization of the multiple equilibria regime in a global ocean model. *Tellus A: Dynamic Meteorology and Oceanography*, **59 (5)**, 695–705.
- Dijkstra, H. A., 2023: The role of conceptual models in climate research. *Physica D: Nonlinear Phenomena*, 133984.
- Ditlevsen, P., and S. Ditlevsen, 2023: Warning of a forthcoming collapse of the Atlantic meridional overturning circulation. *Nature Communications*, **14 (1)**, 4254.
- Doedel, E. J., R. C. Paffenroth, A. C. Champneys, T. F. Fairgrieve, Y. A. Kuznetsov, B. E. Oldeman, B. Sandstede, and X. J. Wang, 2007: AUTO-07p: Continuation and Bifurcation Software for Ordinary Differential Equations.
- Doedel, E. J., R. C. Paffenroth, A. C. Champneys, T. F. Fairgrieve, Y. A. Kuznetsov, B. E. Oldeman, B. Sandstede, and X. J. Wang, 2021: auto-07p. URL <https://github.com/auto-07p/auto-07p>.
- Garzoli, S. L., M. O. Baringer, S. Dong, R. C. Perez, and Q. Yao, 2013: South Atlantic meridional fluxes. *Deep Sea Research Part I: Oceanographic Research Papers*, **71**, 21–32.
- Hawkins, E., R. S. Smith, L. C. Allison, J. M. Gregory, T. J. Woollings, H. Pohlmann, and B. De Cuevas, 2011: Bistability of the Atlantic overturning circulation in a global climate model and links to ocean freshwater transport. *Geophysical Research Letters*, **38 (10)**, L10 605.
- Hu, A., and Coauthors, 2012: Role of the Bering Strait on the hysteresis of the ocean conveyor belt circulation and glacial climate stability. *Proceedings of the National Academy of Sciences*, **109 (17)**, 6417–6422, <https://doi.org/10.1073/pnas.1116014109>.

- Huisman, S. E., M. Den Toom, H. A. Dijkstra, and S. Drijfhout, 2010: An indicator of the multiple equilibria regime of the atlantic meridional overturning circulation. *Journal of Physical Oceanography*, **40** (3), 551–567.
- Jackson, L. C., A. Biastoch, M. W. Buckley, D. G. Desbruyères, E. Frajka-Williams, B. Moat, and J. Robson, 2022: The evolution of the North Atlantic meridional overturning circulation since 1980. *Nature Reviews Earth & Environment*, **3** (4), 241–254.
- Jacques-Dumas, V., R. M. van Westen, F. Bouchet, and H. A. Dijkstra, 2023: Data-driven methods to estimate the committor function in conceptual ocean models. *Nonlinear Processes in Geophysics*, **30** (2), 195–216.
- Lestang, T., F. Ragone, C.-E. Bréhier, C. Herbert, and F. Bouchet, 2018: Computing return times or return periods with rare event algorithms. *Journal of Statistical Mechanics: Theory and Experiment*, **2018** (4), 043 213.
- Lin, Y.-J., B. E. Rose, and Y.-T. Hwang, 2023: Mean state AMOC affects AMOC weakening through subsurface warming in the Labrador Sea. *Journal of Climate*, **36** (12), 3895–3915.
- Lohmann, J., and P. D. Ditlevsen, 2021: Risk of tipping the overturning circulation due to increasing rates of ice melt. *Proceedings of the National Academy of Sciences*, **118** (9), e2017989 118, <https://doi.org/10.1073/pnas.2017989118>.
- Marotzke, J., 2000: Abrupt climate change and thermohaline circulation: Mechanisms and Predictability. *Proc. Natl. Acad. Sci.*, **97**, 1347–1350.
- Mecking, J., S. Drijfhout, L. Jackson, and M. Andrews, 2017: The effect of model bias on Atlantic freshwater transport and implications for AMOC bi-stability. *Tellus A: Dynamic Meteorology and Oceanography*, **69** (1), 1299 910.
- Mehling, O., R. Börner, and V. Lucarini, 2023: Limits to predictability of the asymptotic state of the Atlantic Meridional Overturning Circulation in a conceptual climate model. *arXiv preprint arXiv:2308.16251*.
- Orihuela-Pinto, B., M. H. England, and A. S. Taschetto, 2022: Interbasin and interhemispheric impacts of a collapsed atlantic overturning circulation. *Nature Climate Change*, **12** (6), 558–565.

- Peltier, W. R., and G. Vettoretti, 2014: Dansgaard-Oeschger oscillations predicted in a comprehensive model of glacial climate: A “kicked” salt oscillator in the Atlantic. *Geophysical Research Letters*, **41** (20), 7306–7313.
- Rahmstorf, S., and Coauthors, 2005: Thermohaline circulation hysteresis: a model intercomparison. *Geophysical Research Letters*, **L23605**, 1–5.
- Smeed, D. A., and Coauthors, 2018: The North Atlantic Ocean is in a state of reduced overturning. *Geophysical Research Letters*, **45** (3), 1527–1533.
- Stommel, H., 1961: Thermohaline convection with two stable regimes of flow. *Tellus*, **13** (2), 224–230.
- van Westen, R. M., and H. A. Dijkstra, 2023: Asymmetry of AMOC Hysteresis in a State-of-the-Art Global Climate Model. *Geophysical Research Letters*, **50** (22), e2023GL106088.
- van Westen, R. M., M. Kliphuis, and H. A. Dijkstra, 2024: Physics-Based Early Warning Signal shows AMOC is on Tipping Course. *Science Advances*, *in press*, 1–29.
- Vettoretti, G., and W. R. Peltier, 2016: Thermohaline instability and the formation of glacial North Atlantic super polynyas at the onset of Dansgaard-Oeschger warming events. *Geophysical Research Letters*, **43** (10), 5336–5344.
- Weijer, W., W. Cheng, O. A. Garuba, A. Hu, and B. T. Nadiga, 2020: CMIP6 Models Predict Significant 21st Century Decline of the Atlantic Meridional Overturning Circulation. *Geophysical Research Letters*, **47** (12), e2019GL08607, <https://doi.org/10.1029/2019gl086075>.
- Worthington, E. L., B. I. Moat, D. A. Smeed, J. V. Mecking, R. Marsh, and G. D. McCarthy, 2021: A 30-year reconstruction of the Atlantic meridional overturning circulation shows no decline. *Ocean Science*, **17** (1), 285–299.
- Yang, J., and J. D. Neelin, 1993: Sea-ice interaction with the thermohaline circulation. *Geophys. Res. Letters*, **20**, 217 – 220.